PAPER • OPEN ACCESS

Dynamic evolution of periodic collapse and carbon impurity distribution at the plasma boundary with magnetic islands on J-TEXT

To cite this article: Jiankun Hua *et al* 2026 *Nucl. Fusion* **66** 016033

OPEN ACCESS
IOP Publishing | International Atomic Energy Agency
Nuclear Fusion
Nucl. Fusion **66** (2026) 016033 (14pp)
https://doi.org/10.1088/1741-4326/ae18e5

Dynamic evolution of periodic collapse and carbon impurity distribution at the plasma boundary with magnetic islands on J-TEXT

Jiankun Hua[1,2], Yunfeng Liang[1,2,3,*], Zhonghe Jiang[1], Song Zhou[1], Jie Yang[4], Feiyue Mao[1], Zhengkang Ren[1], Qinghu Yang[1], Nengchao Wang[1] and the J-TEXT Team[1]

[1] State Key Laboratory of Advanced Electromagnetic Technology, International Joint Research Laboratory of Magnetic Confinement Fusion and Plasma Physics, School of Electrical and Electronic Engineering, Huazhong University of Science and Technology, Wuhan 430074, China
[2] Forschungszentrum Jülich GmbH, Institute of Fusion Energy and Nuclear Waste Management, Jülich 52425, Germany
[3] Institute of Plasma Physics, Chinese Academy of Sciences, 23003 Hefei, China
[4] Institute of Metal Research, Chinese Academy of Sciences, 110000 Shenyang, China

E-mail: y.liang@fz-juelich.de

Received 5 August 2025, revised 22 October 2025
Accepted for publication 29 October 2025
Published 25 November 2025

Abstract

Periodic collapses at the edge of Ohmic-mode plasma under Resonant Magnetic Perturbation (RMP) have been observed in the J-TEXT tokamak. These collapses occur following the field penetration. During the collapse, particles and heat flow outward through the X-point of the boundary $m/n = 3/1$ magnetic island, where m and n are the poloidal and toroidal mode number respectively. After the collapse, the magnetic island rapidly expands to its maximum width, then gradually shrinks until it disappears. The reason why the magnetic island cannot sustain itself remains unclear. Afterward, the edge plasma returns to its initial state, and the cycle will repeat with the next collapse. Additionally, the conditions leading to periodic collapses have been identified, the amplitude of RMPs at $q = 3$ resonant surface is essential. No field penetration exists if the amplitude is too small. If the amplitude is too large, the magnetic island remains after field penetration and collapses no longer happen. Therefore, periodic collapses only appear when applying a moderate amplitude of RMP. Carbon impurities play a significant role in triggering instabilities of edge magnetic island and collapse events. This behavior is different from the pumping-out effect previously observed on J-TEXT, which was caused by a 2/1 magnetic island in the core.

* Author to whom any correspondence should be addressed.

Keywords: collapse, RMPs, magnetic island, carbon impurities

(Some figures may appear in colour only in the online journal)

1. Introduction

It has been widely observed that collapse activities occur in magnetic confinement devices, e.g. sawtooth crashes [1], major disruptions [2] and edge-localized-modes (ELMs) [3]. These activities frequently impact the stable operation of devices, making it essential to either suppress or control them. Among these, the control of ELMs is a particularly prominent issue, especially for the International Thermonuclear Experimental Reactor (ITER). ELMs can cause periodic collapses in the pedestal region of the H-mode, releasing a substantial amount of energy outward. Particularly, Type-I ELMs [4] significantly contribute to the loss of confinement and the severe damage to plasma-facing components.

Resonant Magnetic Perturbation (RMP) have been employed as an effective method to control ELMs across in many devices [5–10]. On one hand, it is believed that the edge topological changes induced by RMPs play an important role [11] in suppressing or mitigating ELMs. On the other hand, the boundary conditions will affect the plasma response and effectiveness of RMPs in controlling ELMs [12]. On JET, the $n = 2$ field has little or no effect on ELMs when using a carbon wall in the high collisionality plasma region. However, with an ITER-like wall, it can increase the frequency of ELMs and cause splitting of strike points. The plasma-wall interaction and edge impurity behavior can significantly affect the plasma's response to RMP, ultimately leading to different effects on ELMs.

The edge three-dimensional magnetic topology can help regulate stability at the boundary. In some cases, however, it is inherently unstable. Unlike tokamak devices with RMPs, stellarator devices naturally exhibit magnetic island chains at the plasma boundary. The magnetic island chains can be cut by target as island divertor. On LHD [13], a type of self-sustained divertor oscillation of the $n/m = 1/1$ magnetic island at the plasma boundary is discovered. The oscillation can be explained as the competition of width of $n/m = 1/1$ magnetic island and the bootstrap current localized near X-point during detachment-attachment transitions. Otherwise, the $n/m = 5/5$ magnetic islands will experience periodic collapses if they are just located inside the last closed flux surface (LCFS) on W7-X [14]. These observations imply the edge magnetic islands will become unstable in some cases, and this will affect the stable operation of devices, especially for detachment operation [15].

It has also been reported in NSTX that pedestal collapse can be triggered by RMPs pulse during ELMs-free periods [9]. Recently, the edge periodic collapse events are also observed on J-TEXT Ohmic-mode plasma with RMPs and a graphite target. This suggests the instability of the edge three-dimensional magnetic topology is a common phenomenon, regardless of whether for tokamak devices or stellarator devices. Meanwhile, collapse can occur even in the plasma boundary without a pedestal region. The measurements of plasma profile and carbon impurity on J-TEXT can provide dynamic evolution of collapse events, which may shed new light on the mechanism behind collapse or the effect of RMPs on collapse behavior.

In the rest part of the paper, the experimental setup is described in section 2. In section 3, the experimental observation is given: the dynamic evolution of periodic RMPs-induced collapse is presented in section 3.1, the impact of RMPs phase on the collapse is shown in section 3.2, section 3.3 give the condition of collapse induced by RMP. Sections 4 and 5 give the discussion and conclusion.

2. Experimental setups

The J-TEXT is a conventional, middle-sized tokamak with a major radius $R = 1.05$ m and a minor radius $r = 0.2$–0.29 m [16]. The RMPs coils system on J-TEXT includes 24 in-vessel saddle coils [17]. The system can generate static RMPs with different dominant resonant components by adjusting the current ratios of saddle coils. In the present experiments, a dominant $m/n = 3/1$ component is produced with an edge safety factor $q_a > 3$. The 3/1 component at the plasma edge is about 1.09 Gauss per kilo-ampere of coil current, based on calculations performed under the vacuum assumption.

Figure 1 shows an overview of the diagnostics used in this study. The electron density is measured by multi-channel laser-based polarimeter-interferometer [18] at Port 11. The electron temperature is determined by electron cyclotron emission (ECE) system [19] at Port 09. Two identical photodiode arrays are employed to measure carbon III (CIII) emission and H_α emission [20] at Port 10. The locked mode detectors consist of two sets of saddle loops, and each set includes two loops installed at two opposite toroidal locations outside of the vacuum vessel [21]. It can measure the magnetic perturbation with odd toroidal mode number. The magnetic fluctuations are measured by a set of 16 toroidal Mirnov probes, which is distributed uniformly in the toroidal direction on the low-field-side (LFS) [21]. A microwave Doppler backscattering (DBS) system is used to measure the perpendicular velocity of edge plasma at Port 02 [22]. There are four limiters on J-TEXT. The high-field-side (HFS) limiter is a toroidal symmetry target, which is generally used for poloidal divertor configuration [23]. While the limiters on the LFS, top and bottom are localized limiters, each covering less than 10 degrees in the toroidal direction. These three localized limiters are installed at port 14. During experiments, the plasma is usually limited by the HFS target, and all limiters

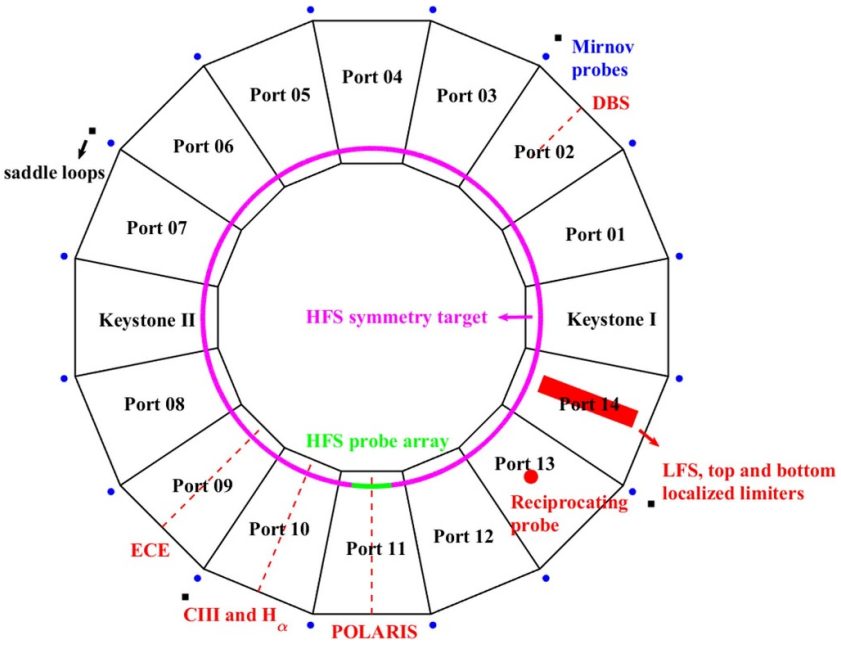

Figure 1. Layout of plasma diagnostics on J-TEXT.

are made of graphite. As a result, carbon is the primary impurity in the J-TEXT tokamak. Thirteen sets of limiter probes are installed on the HFS target at Port 09. Each set consists of triple probes that measure the floating voltage (V_f) and ion saturated current (I_s). Additionally, a reciprocating probe is employed to measure the edge electron density and temperature at Port13.

3. Observations of the periodic collapses at the plasma boundary on J-TEXT

The periodic edge collapses are characteristic phenomenon typically observed at the pedestal region of H-mode plasmas. However, all discharges analyzed in this study are in Ohmic-mode plasmas. Consequently, the edge periodic collapses observed on J-TEXT are not driven by steep pressure or current gradients at the plasma boundary. Instead, magnetic reconnection induced by RMPs plays a significant role in triggering rapid outward transport. The experimental details are presented as follows.

3.1. Dynamic evolution of edge periodic collapse events on J-TEXT

Figure 2 presents a typical observation of periodic collapse events at the plasma boundary during the discharge #1083048. The plasma is limited by the HFS target. The plasma parameters remain nearly constant before applying the RMPs coils. The toroidal magnetic field B_T is 1.7 T, and the toroidal plasma current I_p is 150 kA. Consequently, the edge safety factor is approximately 3.5 as shown in figure 2(*a*). The RMP coils current I_c is initiated at 0.21 s, and it reaches its peak value (~ -6 kA) at 0.23 s as shown in figure 2(*b*).

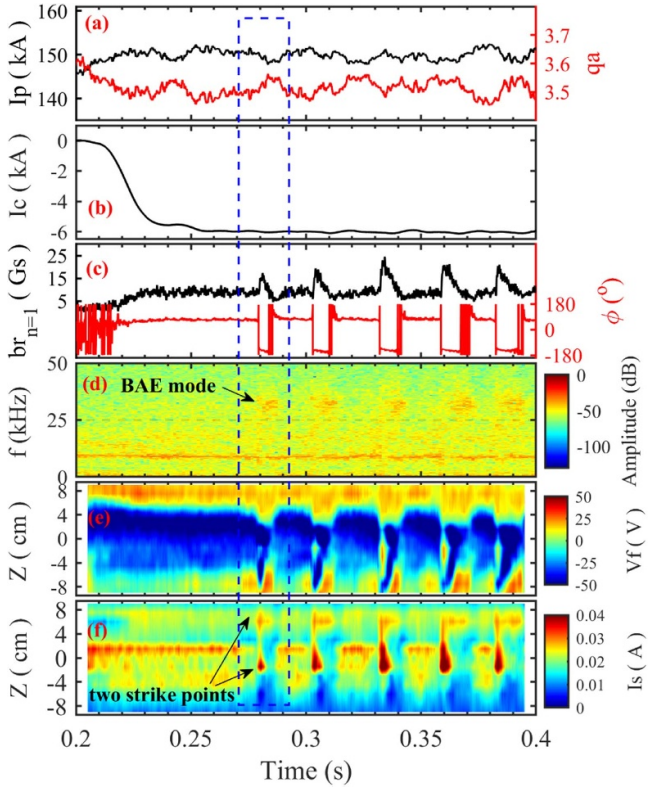

Figure 2. Discharge #1083048: Time evolution of (*a*) $\boldsymbol{I_p}$ and, (*b*) $\boldsymbol{I_c}$, (*c*) $\boldsymbol{b_{r,n=1}}$ and its phase ϕ, (*d*) perturbated magnetic spectrum, (*e*) $\boldsymbol{V_f}$ at the HFS target, (*f*) $\boldsymbol{I_S}$ at the HFS target.

No field penetration occurs before $t = 0.275$s due to the rotation screening effect. Only a linear plasma response to I_c is observed during $t = 0.2$ s ~ 0.275s. This is shown by

radial magnetic perturbation ($b_r^{n=1}$, black curve) in figure 2(c). Meanwhile, the V_f and the I_s measured at the HFS target show almost no obvious change, as indicated in figures 2(e) and (f). These results suggest no magnetic island forms by $t = 0.275$s.

The $b_r^{n=1}$ signal increases sharply, and its phase shifts by 180 degrees at 0.279 s, as shown in figure 2(c). This indicates that the field penetration occurs, leading to the formation of magnetic islands. Sawtooth oscillations still remained in the plasma core, confirming that the observed island is a 3/1 mode rather than a 2/1 mode. Meanwhile, figure 2(d) shows a beta-induced Alfvén Eigenmode (BAE) with a frequency of approximately 35 kHz appears in the perturbated magnetic spectrum. The BAE usually occurs when a 3/1 magnetic island is wide enough on J-TEXT [24–26].

The width of the magnetic island is proportional to $\sqrt{b_r^{n=1}}$ [27]. Once the edge nested magnetic surface is broken, the 3/1 magnetic island expands rapidly to its maximum width. This changes the interaction between the HFS target and the edge plasma, leading to the formation of two strike lines. Two distinct strike points can be observed in the and I_s signal, as shown in figures 2(e) and (f). However, the 3/1 magnetic island is not sustained. It decays immediately and vanished finally between $t = 0.28 \sim 286$s, as indicated by dropping of $b_r^{n=1}$ in figure 2(c). The BAE mode disappears as well. Two strike points move in response to the evolution of the 3/1 magnetic island. Finally, the plasma returns to the original limiter configuration until the next field penetration. An evolution cycle is outlined by the blue dotted rectangle.

For this discharge, the plasma pressure and safety-factor (q) profiles were obtained from EFIT reconstruction as shown in figure 3. The $q = 3$ rational surface is located at $r = 0.237$ m. Figure 4 shows the time history of plasma parameters in detail during one cycle of this discharge. Figures 4(a) and (b) display the rapid growth ($t = 0.279$ s ~ 0.28 s), slow decay ($t = 0.28$ s ~ 0.285 s), and disappearance of the 3/1 magnetic island within this cycle. As a result, the strike point at the HFS target undergoes splitting and recovery, as shown in figure 4(c). Figure 4(d) illustrates that the core electron density and temperature remained almost unchanged during this process.

During the magnetic island growth phase, the edge electron density and temperature decreased rapidly inside the $q = 3$ surface, as shown in figures 4(e) and (g). In contrast, they increased rapidly outside the $q = 3$ surface, as shown in figures 4(f) and (h). These observations suggest that this phase involves enhanced particle and heat transport, with a collapse reversal surface for rapid transport located near the $q = 3$ surface. Therefore, we define this phenomenon as a periodic edge collapse event, and the location of collapse is near the $q = 3$ surface. It takes place at the moment of field penetration. Following this phase, the island decays slowly until it vanishes completely at $t = 0.285$s. The electron density and temperature inside $q = 3$ surface will recover to original state after disappearance of the island.

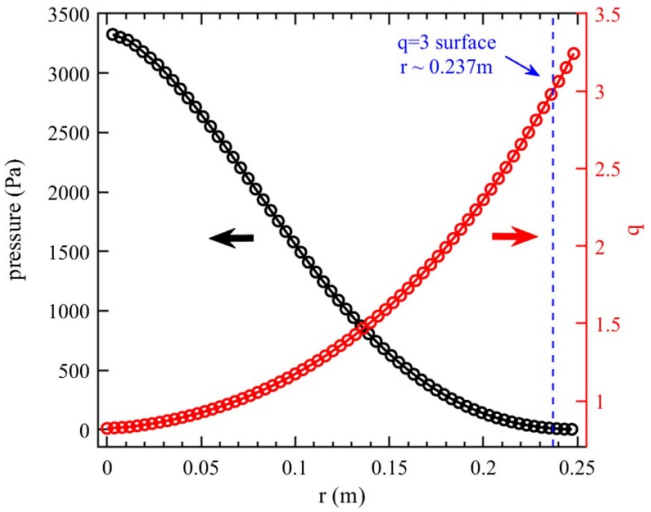

Figure 3. Plasma pressure and q profile from EFIT for discharge #1083048.

3.2. *The impact of RMPs phase on the collapse*

As mentioned in figure 4, the collapse occurs at the moment of field penetration. This suggests the collapse may be related to magnetic reconnection driven by RMPs. Typically, the outward transport flows rapidly across the X point of the magnetic island during magnetic reconnection process. Therefore, although the collapse reverse surface is speculated to be located at the $q = 3$ surface, the actual poloidal location of radial outward transport should depend on the position of the X point. In other words, the location of rapid outward transport is expected to depend on the phase of applying RMPs.

Two RMP phases, differing by 180 degrees, are compared in this experiment, as show in figure 5. Figures 5(a) and (b) present Poincaré plots at the Port 11 cross section, which are calculated under the vacuum assumption with actual RMP coils' currents. The density measurement channels are indicated by solid lines in figures. Although these plots may not accurately represent the actual magnetic topology, they can still provide approximate locations of X points and O points of the 3/1 magnetic islands after field penetration. The contour plots of perturbated electron density evolution are shown in figures 5(c) and (d). For the discharge #1083048, the boundary channels primarily pass through the 3/1 magnetic island. The electron density within the magnetic island decreased rapidly, while the electron density at the scrape-off layer ($R > 1.26$ m) increase slightly after collapse. For the discharge #1083046, the phase of the 3/1 magnetic island is reversed. Accordingly, the channels marked by yellow line pass through the X-point of 3/1 magnetic island. The electron density near X-point increase rapidly during the collapse. Especially, the core channels show a rapid decrease. It is important to note that the density measurements are chord-integrated. The observed variation in the core channel signal may be attributed mainly by changes at the boundary, because the core channel pass through the boundary 3/1 magnetic island.

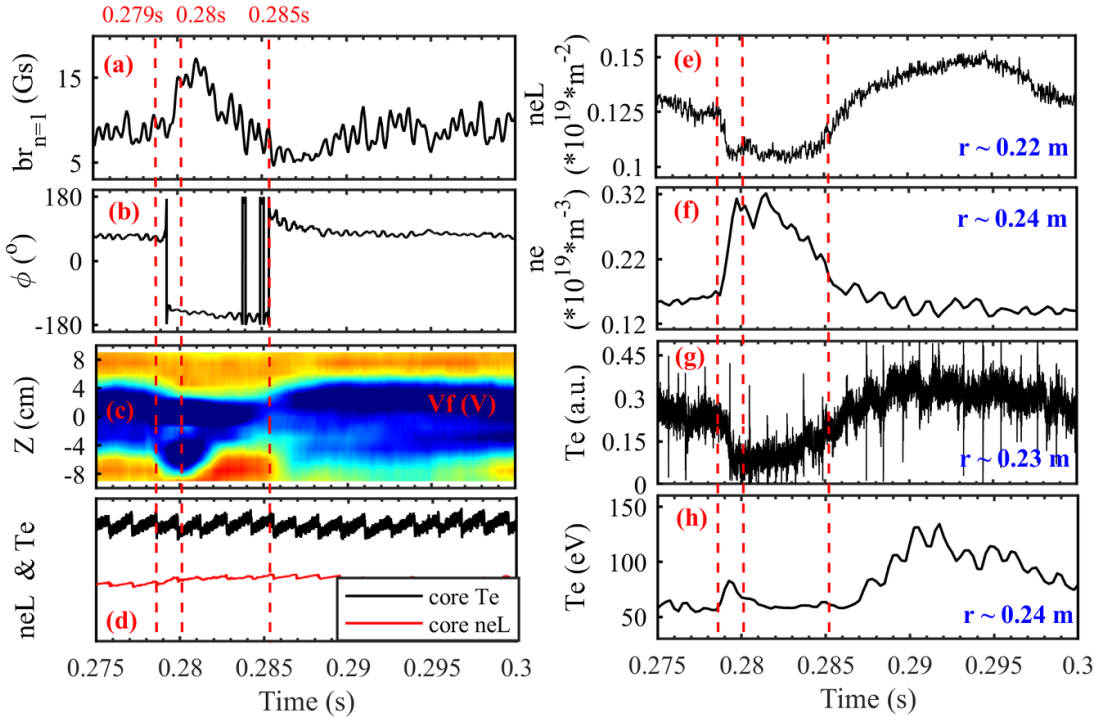

Figure 4. Discharge #1083048. Time history of (*a*) $\boldsymbol{b_r^{n=1}}$, (*b*) the phase of $\boldsymbol{b_r^{n=1}}$ (*c*) Vf in HFS target, (*d*) core electron temperature and density, (*e*) $\boldsymbol{n_{eL}}$ at $r = 0.22$ m, (*f*) $\boldsymbol{n_e}$ at $r = 0.24$ m, (*g*) $\boldsymbol{T_e}$ at $r = 0.23$ m, (*h*) at $r = 0.24$ m. Especially, the $\boldsymbol{n_e}$ and $\boldsymbol{T_e}$ at $r = 0.24$ m is measured by reciprocating probe, the position of probe keeps $r = 0.24$ m during this collapse event.

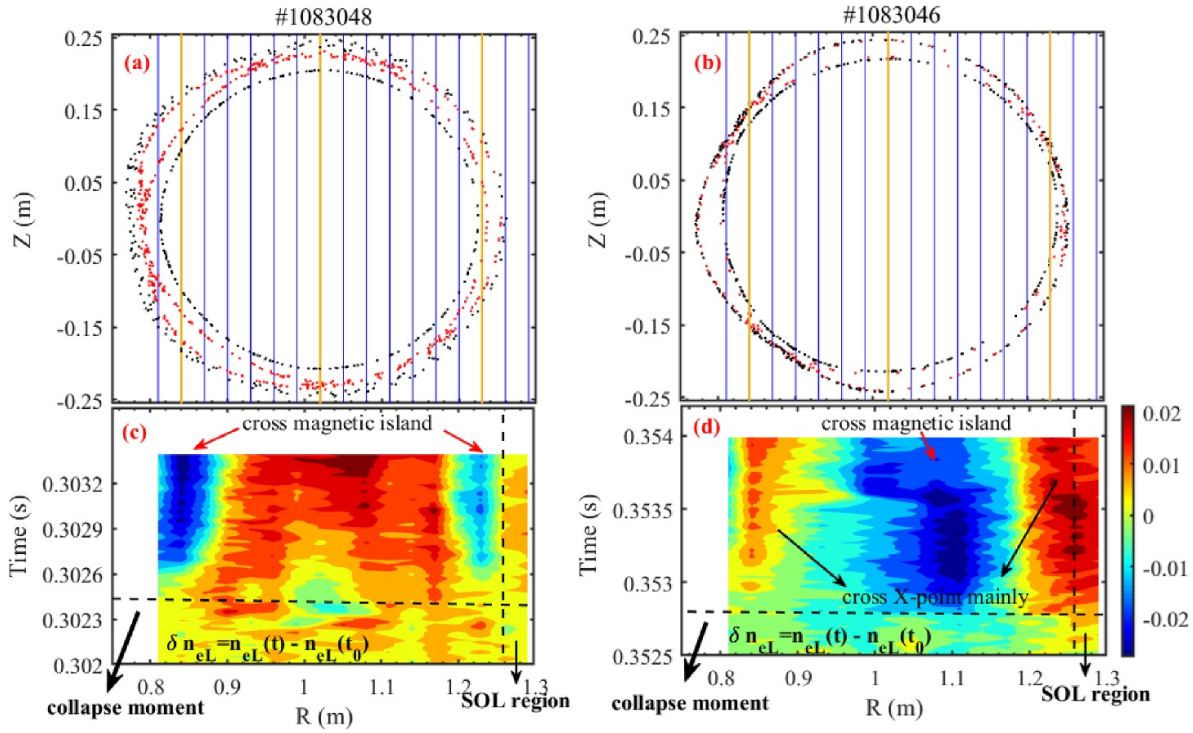

Figure 5. Poincaré plots for (*a*) #1083048 at $t = 0.3024$ s and (*b*) #1083046 at $t = 0.3528$ s at the Port 11 cross section. The solid lines represent the line of sight for density measurement, and the time history of electron density along yellow lines are shown in figure 6. The contour plot of $\boldsymbol{\delta n_{eL}}$ for (*c*) #1083048 and (*d*) #1083046, $\boldsymbol{t_0}$ is represents the chosen initial time.

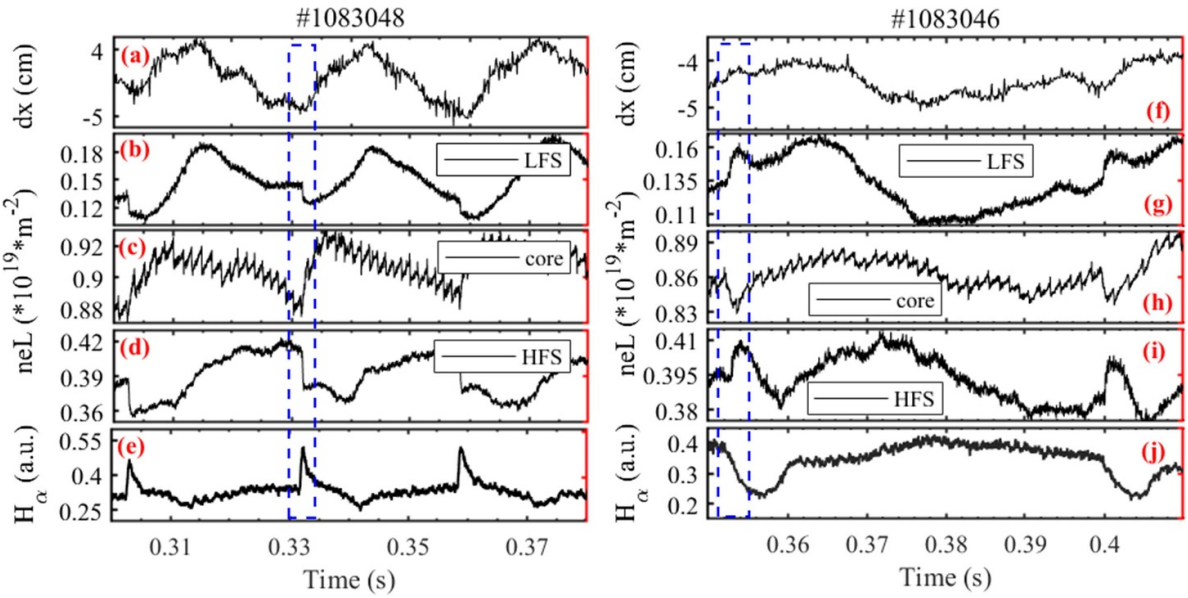

Figure 6. Time evolution of (*a*) horizontal displacement; electron density $\boldsymbol{n_{eL}}$ at (*b*) LFS, (*c*) core and (*d*) HFS; (*e*) particle recycling in the discharge #1083048. Time evolution of (*f*) horizontal displacement; electron density $\boldsymbol{n_{eL}}$ at (*g*) LFS, (*h*) core and (*i*) HFS; (*j*) particle recycling in the discharge #1083046.

The time evolutions of electron density measured by LFS, core and HFS channels are shown in figure 6. These channels correspond to yellow solid lines in figure 5. One cycle is highlighted by the blue rectangle, and this corresponds to the temporal evolution of the perturbated density shown in figures 5(*c*) and (*d*). During the cycle, the horizontal displacement of the plasma may exhibit some variations as show in figures 6(*a*) and (*f*). However, the slow evolution of the horizontal displacement is clearly distinguishable from the rapid transport behavior associated with the collapse. Figures 6(*e*) and (*j*) show the time evolutions of the fueling particle recycling, which are measured from an HFS edge H_α channel. They also show different trends of evolution during the collapse process for these two discharges. In the discharge #1083048, each collapse was accompanied by a burst-like increase in the H_α sign. The H_α signal begins to decrease after crash. However, in the discharge #1083046, no significant change in the H_α signal at the moment of the collapse. And then, the H_α signal also begins to decrease after crash. The different behaviors are attributed to the phase of the magnetic island.

Figure 7 shows Poincaré plots at the Port 10 cross section, the lines of sight for H_α measurement are indicated by yellow solid lines. In this toroidal cross-section, the X-point of the magnetic island is near the HFS target after field penetration for #1083048. As a result, particles are transported outward through the X point and strike the HFS target after crash. This causes a backflow of particles into the plasma from a nearby location. In contrast, the O-point of the magnetic island is near the HFS target in this cross section for #1083046. In this case, no backflow is observed.

Figure 8 illustrates the detailed evolution of the particle recycling profile before and after the collapse. Four time points are selected, $t_0 \sim t_3$. t_0 represents a time point before the collapse. t_1 represents a time point immediately after the collapse. t_2 represents a time point during the evolution of the magnetic island. And t_4 represents a time point after the disappearance of the magnetic island. In the discharge #1083048, the X-point of the magnetic island approaches the HFS target when the field penetration occurred. At the moment of the field penetration, the H_α profile increases overall. Subsequently, although the magnetic island continues to grow, the H_α profile gradually declines. It eventually returns to its initial state when the magnetic island disappears. In the discharge #1083046, H_α profile slightly decreases at the moment of the field penetration. It continued to decline during the presence of the magnetic island and eventually returned closed to its initial level after the island disappeared.

The evolution of density and particle cycling both suggest that at the moment of field penetration, particles inside the $q = 3$ surface were rapidly transported through the X-point, triggering the edge collapse. After the collapse, the magnetic island gradually increased to its maximum width. The density profile is related to the level of edge particle cycling, which is discuss in [28]. Afterward, the 3/1 magnetic island slowly decays and eventually disappears, and both the plasma density and particle recycling return to its initial state.

Since all ECE channels are located within the $q = 3$ surface in this experiment, it cannot be distinguished that the dependence of electron temperature evolution on the RMP phase during the collapse from ECE signals. However, the heat transport is likely consistent with the particle transport.

3.3. The condition of collapse

As mentioned above, the collapse or rapid radial transport is closely related to 3/1 field penetration or magnetic reconnection at the plasma boundary. Therefore, a specific RMP amplitude at the $q = 3$ resonant surface is required. In the following

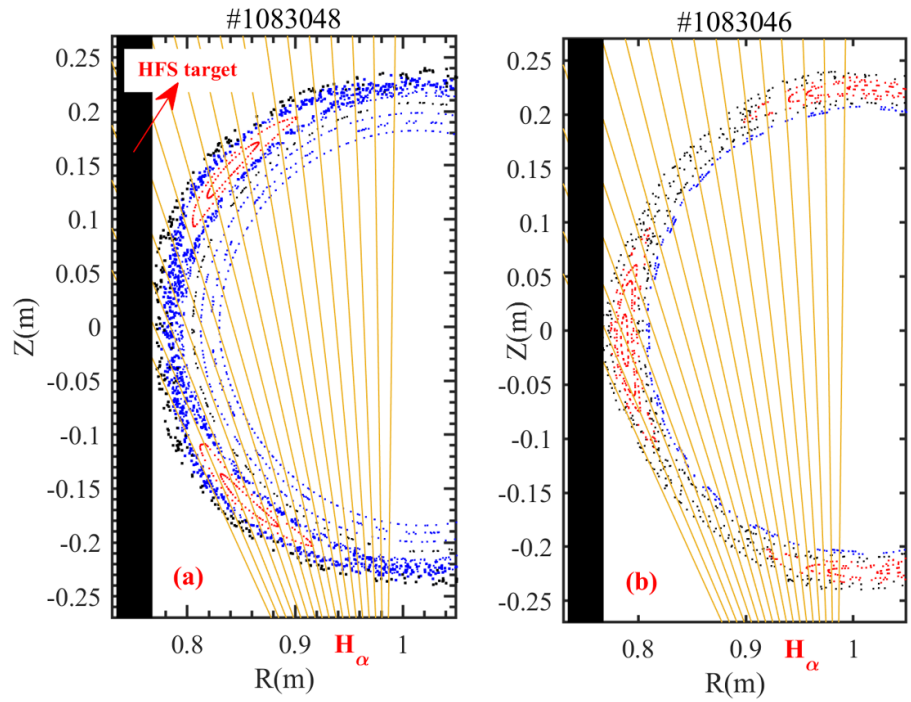

Figure 7. Poincaré plots for (*a*) #1083048 at t = 0.3024 s and (*b*) #1083046 at t = 0.3528 s at the Port 11 cross section.

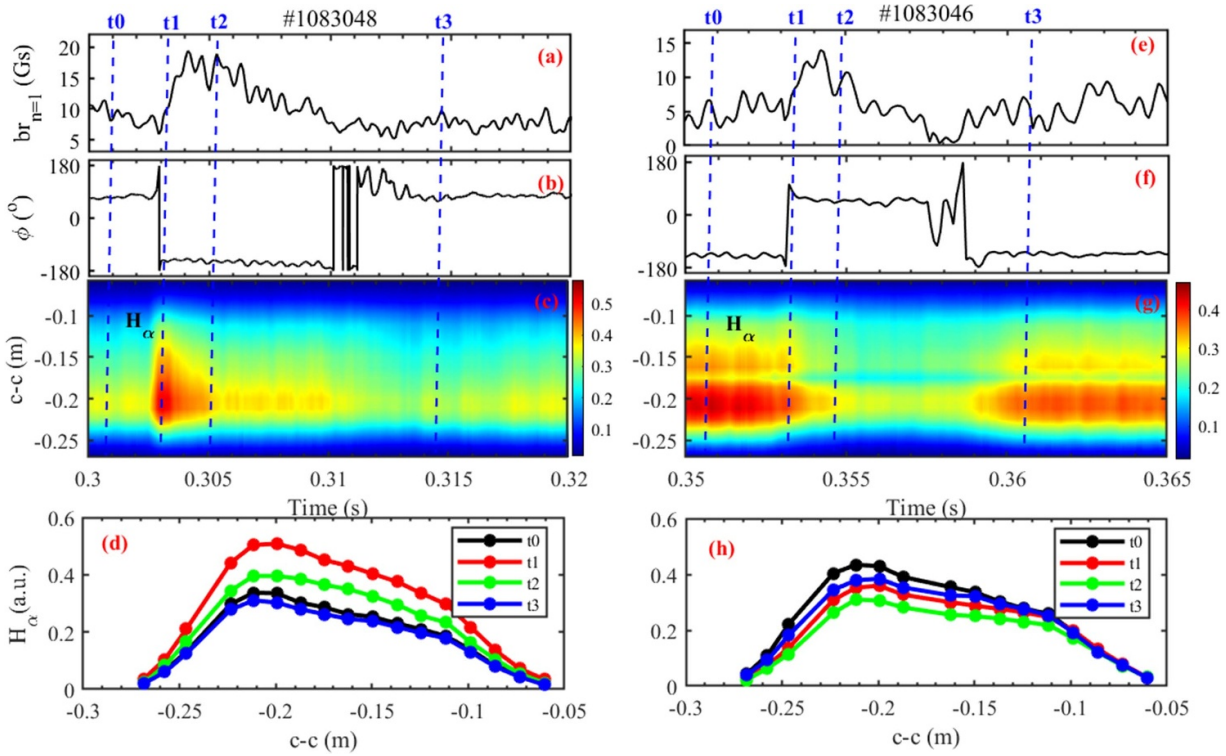

Figure 8. Time history of (*a*) $\boldsymbol{b_r}$, (*b*) the phase of $\boldsymbol{b_r}$, (*c*) $\boldsymbol{H_\alpha}$ signal, the c-c is chord-to-center distance. (*d*) $\boldsymbol{H_\alpha}$ signal profile in different moments in the discharge #1083048. Time history of (*e*) $\boldsymbol{b_r}$, (*f*) the phase of $\boldsymbol{b_r}$, (*g*) $\boldsymbol{H_\alpha}$ signal. (*h*) $\boldsymbol{H_\alpha}$ signal profile in different moments in the discharge #1083046.

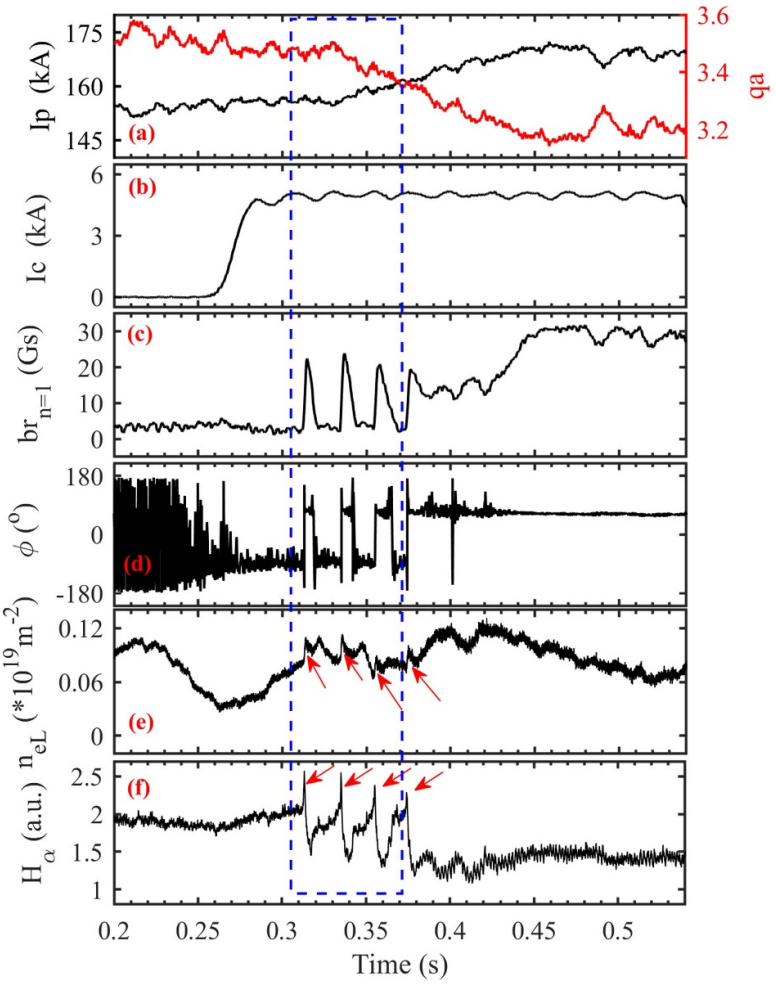

Figure 9. Time history of (*a*) $\boldsymbol{I_p}$ and $\boldsymbol{q_a}$, (*b*) $\boldsymbol{I_c}$, (*c*) $\boldsymbol{b_{r,n=1}}$, (*d*) the phase of $\boldsymbol{b_{r,n=1}}$, (*e*) $\boldsymbol{n_{eL}}$ and (*f*) $\boldsymbol{H_\alpha}$ in the discharge #1077700.

analysis, the q_a window and the amplitude of RMP are scanned separately.

3.3.1. Dependency on the edge safety factor. In the discharge #1077700, a scan of q_a is conducted by increasing I_p while keeping $B_T = 1.7T$, as illustrated in figure 9(*a*). The I_c ramps up to 4 kA from $t = 0.26$ s to $t = 0.28$ s, and it is maintained for the whole discharge, as shown in figure 9(*b*). Three instances of field penetration and collapse occur between $t = 0.303$ s and $t = 0.375$ s (q_a decreases from 3.46 to 3.35). This is outlined by blue dotted line. In this process, the $q = 3$ resonant surface moves outward as q_a decreases. On one hand, this enhances the amplitude of the 3/1 RMP at the resonant surface. On the other hand, it leads to the 3/1 magnetic island (after field penetration) to be cut deeper.

The final field penetration and collapse occur at $t = 0.374$ s, and the 3/1 magnetic island no longer disappears afterward. The width of the 3/1 magnetic island begins to grow as q_a decreases after $t = 0.39$ s, and remains nearly constant when q_a keeps unchanged, as shown in figures 9(*c*) and (*d*). Figures 9(*e*) and (*f*) present the evolution of electron density and particle recycling. During periodic collapse, burst-like behaviors are observed in both signals. When 3/1 magnetic island is located stably at the plasma boundary after $t = 0.39$ s, the particle recycling remains almost unchanged. The density slowly decreases as decreasing q_a, which may be attributed to a pump-out effect. In summary, the periodic collapse phenomenon disappears at q_a below 3.35. A stable island divertor configuration is established [29]. This q_a threshold of collapse phenomenon has been observed consistently in multiple discharges, indicating good reproducibility.

3.3.2. Dependency on the amplitude of RMP. In the discharge #1083042, the is scanned from 5.2 kA to 6.5 kA with a fixing $q_a = 3.55$, as illustrated in figure 10. Three collapse events occur during $t = 0.27$ s ~ 0.35 s. When the I_c exceeds 6 kA, the magnetic islands persist stably after the final field penetration. As a result, the collapse events cease. This is reflected clearly by the evolution of the phase of the $b_{r,n=1}$ signal in figure 10(*d*). Slight oscillations can be observed from the $b_{r,n=1}$ and the H_α signals after $t = 0.35$ s, but they do not significantly affect plasma parameters.

The periodic behavior involves the formation and disappearance of magnetic islands. Scans of q_a and I_c indicate a marginal RMP amplitude at the resonant surface is required. If the amplitude of the RMP at the $q = 3$ resonant surface

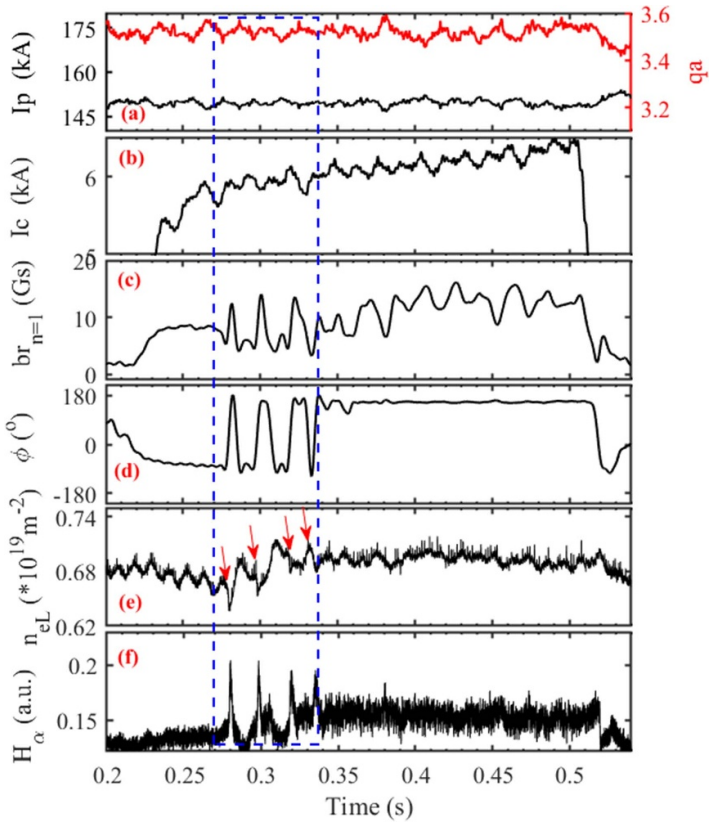

Figure 10. Time history of (*a*) $\boldsymbol{I_p}$ and $\boldsymbol{q_a}$, (*b*) $\boldsymbol{I_c}$, (*c*) $\boldsymbol{b_{r,n=1}}$, (*d*) the phase of $\boldsymbol{b_{r,n=1}}$, (*e*) $\boldsymbol{n_{eL}}$ and (*f*) $\boldsymbol{H_\alpha}$ in the discharge #1083042.

is too low, no field penetration occurs, and consequently, no collapse is triggered. If the amplitude is too high, the edge 3/1 magnetic island remains stable, thereby preventing periodic collapses. Only when the RMP amplitude is moderate, the magnetic island induced by RMP remains marginal stable. As a result, periodic collapses occur, and the magnetic island is unable to persist, disappearing after each collapse.

4. Discussion

Regarding stellarator devices, magnetic island chains naturally persist at the plasma boundary. When the $m/n = 5/5$ magnetic islands are located just inside the LCFS on W7-X, the boundary experiences periodic collapses [14]. The reversal location of the rapid transport is inferred to lie at the X-point of the 5/5 magnetic island chain. Such burst-like event is named as island located modes. Additionally, the nature of this instability transitions from collapse to oscillations during the iota scan. This phenomenon is similar to the magnetic island dynamics observed in the J-TEXT tokamak. These observations suggest that the edge magnetic island instability is a widespread phenomenon. It may even affect the stable detached operation in magnetic island divertor configurations [15, 30].

Figure 11 illustrates the correlation between the collapse and the evolution of the magnetic island on J-TEXT. Firstly, the collapse is accompanied by field penetration. The field penetration here is different from the observation about the excitation of the 2/1 magnetic island on J-TEXT in the past. The collapse or fast radial outward transport discussed here is also different from the pump-out phenomenon after the 2/1 magnetic island [31]. Secondly, the collapse does not occur when the width of the magnetic island become its maximum, but rather when the magnetic island is just beginning to grow. As illustrated in figure 4, this point has already been addressed. Typically, this is when the magnetic reconnection rate is at its maximum, which may lead to a rapid transport in the reconnection region (X-point). In [32], it has been illustrated that the X-point of an island could collapse once the width of the island exceeds a certain critical value $1/\Delta'$, provided that the tearing mode stability parameter, Δ' is sufficiently large. This means the collapse can happen though the width of island is narrow. The secondary structures resulting from the collapse of the X-point at the $q = 2$ surface have been observed on TEXTOR [33]. The observations on J-TEXT may result from a similar mechanism.

However, intrinsic Δ' is typically negative at the $q = 3$ surface for tokamak devices in general. On one hand, the application of RMP will alter Δ'. On the other hand, Δ' could be altered by impurities from the first wall.

It has been observed on the influence of low-Z impurity on 2/1 tearing mode in EAST [34], and 3D resistive MHD simulation has reproduced the process [35]. The accumulation of impurity at edge following a field penetration will have a cooling effect there [36]. This cooling effect provides a

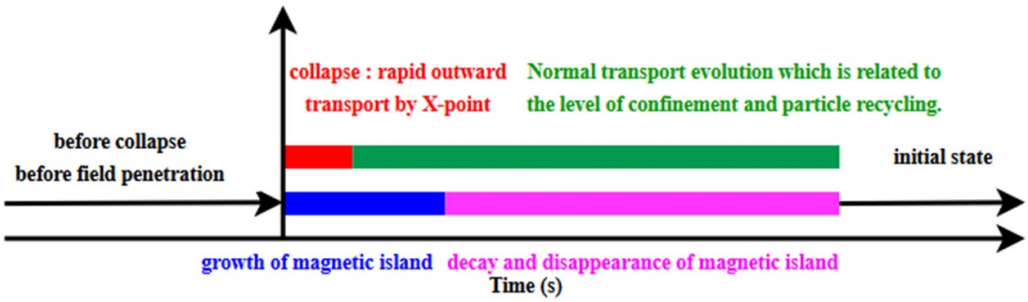

Figure 11. Dynamic evolution of RMPs-induced collapse at the plasma boundary.

destabilizing effect on growth of magnetic island at the plasma boundary, or it will drive a large and positive Δ'.

On one hand, radiation cooling can drive tearing mode instabilities when the radiative power loss exceeds the heating power. In the process of density limit, the $m/n = 2/1$ tearing mode could be driven due to this radiative cooling effect [37–39]. The evolution of radiation-induced tearing modes can be described by adding a radiative term to the modified Rutherford equation [39]:

$$\frac{\mathrm{d}w}{\mathrm{d}t} = C_1 \frac{\eta}{\mu_0}\Delta' - C_2 \frac{\delta P}{\chi_{\perp \mathrm{eff}}^{\mathrm{island}} \langle T_e \rangle} w$$

where w is the island width, Δ' is tearing mode stability parameter, η is the resistivity, μ_0 is the vacuum permeability, C_1 and C_2 are coefficients which vary with the quantities at the rational surfaces. $\langle T_e \rangle$ and $\chi_{\perp \mathrm{eff}}^{\mathrm{island}}$ are the average electron temperature and the perpendicular thermal conductivity inside magnetic islands. δP is the net heating power density, the different between heating power and radiation power loss. As a result when δP is negative, the growth rate is large than zero which drive the growth of the island.

On the other hand, when the finite width of the magnetic island is taken into account, the local current distribution is modified accordingly. In [40], a modified Rutherford equation is proposed:

$$\frac{\mathrm{d}w}{\mathrm{d}t} = 1.66 \frac{\eta}{\mu_0}\Delta'_{\mathrm{classic}} + \Delta'_A(w) + \Delta'_{\delta j}(w)$$

where $\Delta'_{\mathrm{classic}}$ is the classical term, Δ'_A is the island asymmetry term, and $\Delta'_{\delta j}$ is the current perturbation term. Radiation loss change the temperature and current density profile inside the island, thus modifying the $\Delta'_{\delta j}$ term. Meanwhile, the imbalance between radiation loss and heating also enhances the asymmetry of the current distribution within the magnetic island (Δ'_A term), both will drive an exponential growth of magnetic island. In [41], the effect of radiative cooling effect on Δ' is determined by MHD simulation.

The main impurity species in the J-TEXT tokamak is carbon. Its behavior during periodic collapse is study here. Figures 12(*c*) and (*d*) show the evolution of CIII signals. For both cases, the boundary CIII signals consistently increase during the collapse, regardless of the RMP phase. Figure 13 presents Poincaré plots at the Port 10 cross section, and the lines of CIII sight are drawn in the figures. The evolution of the CIII distribution differs from those of the electron density and particle recycling, both of which depend on the RMP phase. In these two discharges with opposite RMP phases, the HFS boundary CIII signal exhibits a significant increase at the moment of the field penetration (t from $t0$ to $t1$ in figures 12(*d*) and (*h*)). The core signals show a relatively weaker increase. And then, the CIII signal immediately began to decrease. After the disappearance of the magnetic island, the CIII signal returned to its initial level ($t = t2$ in figures 12(*d*) and (*h*)).

As shown in figure 1, there is a toroidally symmetry graphite target installed at the HFS. Therefore, field penetration will alter the interaction between the plasma and the target, leading to the introduction of carbon impurities into the plasma boundary. Since the target is toroidally symmetric, similar effects will be induced regardless of the magnetic island phase.

Figure 14 shows the relationship between the boundary CIII signal and the $b_{r,n=1}$ signal during four collapses in the discharge #1083048. Obviously, after the field penetration, carbon impurities rapidly enter the plasma boundary and reach their maximum concentration ($t_0 \sim t_1$), despite the magnetic island width remaining small. Subsequently, as the magnetic island continues to grow to its maximum width, the carbon impurity concentration changes insignificantly ($t_1 \sim$). Eventually, the magnetic island cannot be sustained and gradually decays, and a corresponding decline in carbon impurity concentration can also be observed ($t_2 \sim t_0$). This suggests that radiative cooling effect is one possible reason to destabilize the edge 3/1 magnetic island by the accumulation of carbon impurities. Finally, this trigger fast transport near X-point of island.

The LFS localized limiter is used usually in the past, and few continuous periodic collapses with 3/1 RMPs have been observed on J-TEXT [42]. Therefore, an experiment involving the movement of the plasma position is conducted in the discharge #1080960, to determine the effect of carbon impurity. Initially, the plasma is limited by the LFS localized limiter and the bottom localized limiter ($\mathrm{d}x = 0$), the toroidal coverage of both limiters is less than 10°. The localized limiters are indicated in figure 1. At 0.2 s, the RMP coils are applied (figure 15(*a*)), and by 0.23 s, the coil current ramps up to its maximum value. At this moment, a stable 3/1 magnetic island is excited at the boundary. The first reversal of the vertical rotation velocity, V_{per}, (figure 15(*e*), by 50 GHz

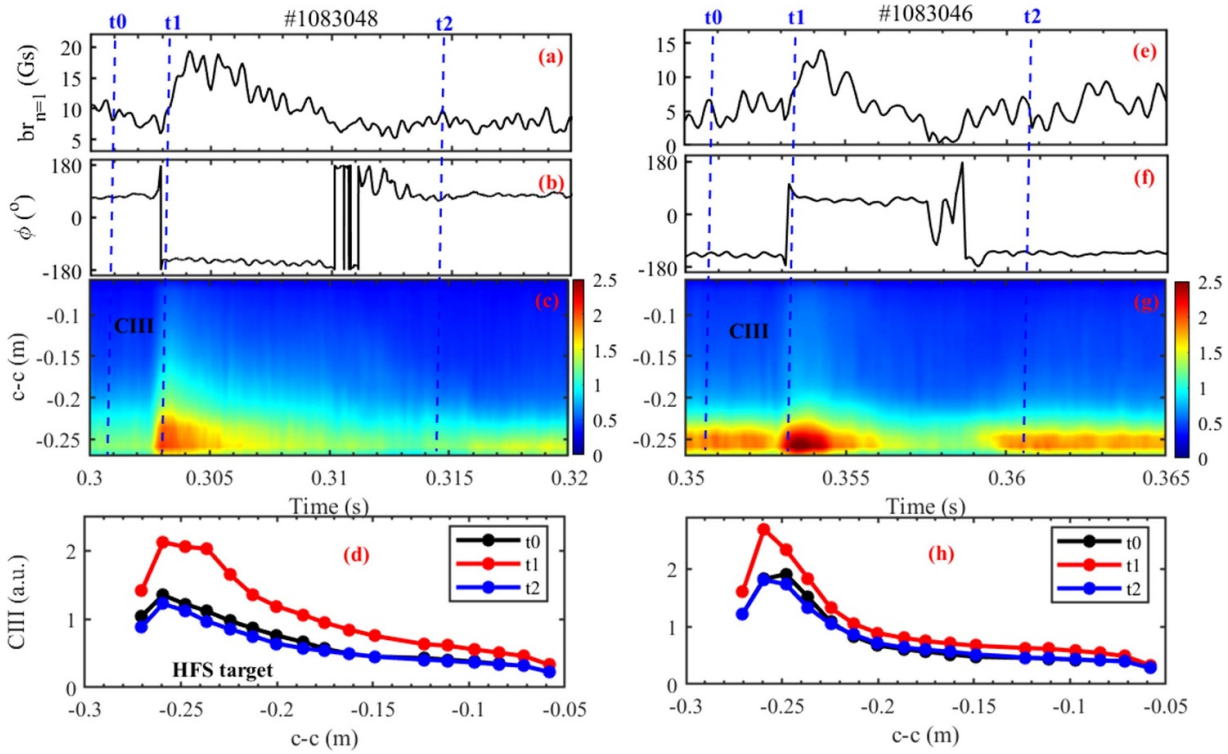

Figure 12. Time history of (*a*) $\boldsymbol{b_r}$, (*b*) the phase of $\boldsymbol{b_r}$, (*c*) CIII signal. (*d*) CIII signal profile in different moments in the discharge #1083048. Time history of (*e*) $\boldsymbol{b_r}$, (*f*) the phase of $\boldsymbol{b_r}$, (*g*) CIII signal. (*h*) CIII signal profile in different moments in the discharge #1083046. The c-c is chord-to-core distance.

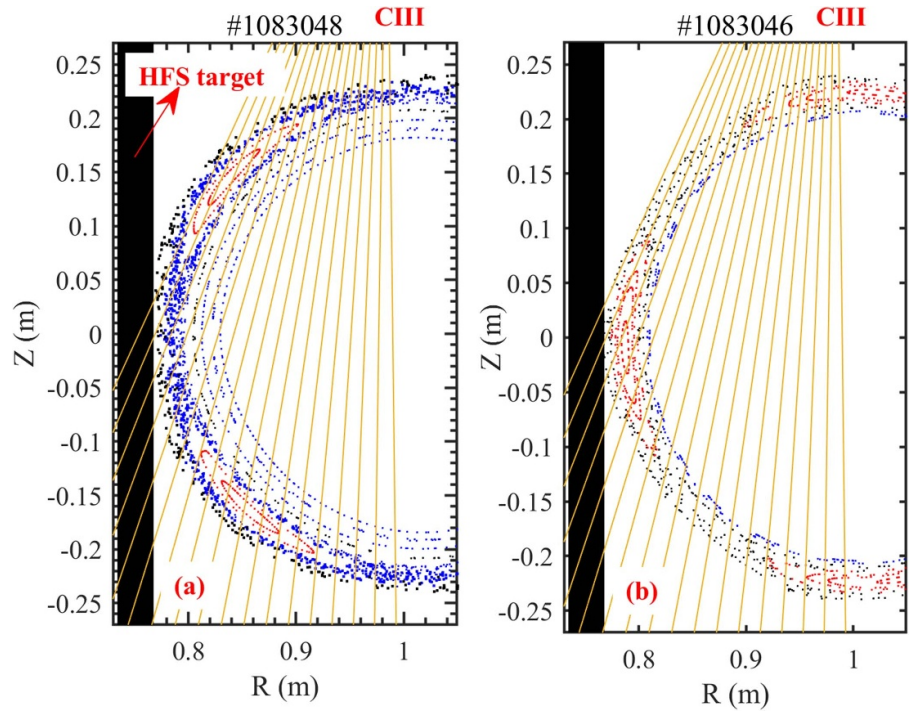

Figure 13. Poincaré plots for (*a*) #1083048 at t = 0.3024 s and (*b*) #1083046 at t = 0.3528 s at the Port 11 cross section.

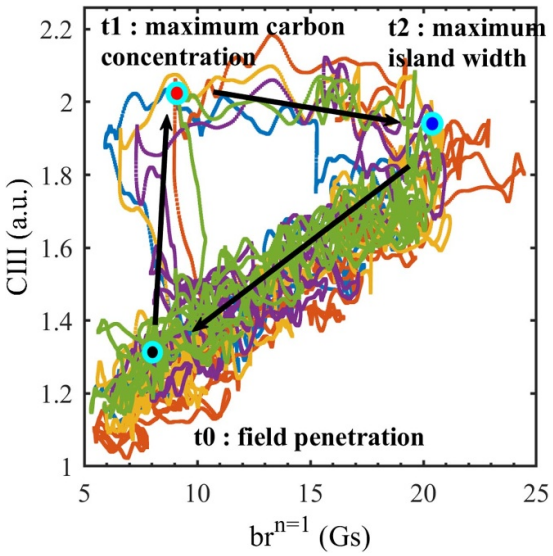

Figure 14. The relation between CIII and $\boldsymbol{b_r}$ during five collapses in the discharge #1083048.

channel) at the boundary is observed. The direction shifts from the electron diamagnetic drift to the ion diamagnetic drift. And a BAE mode with a frequency of approximately 34 kHz is detected in the magnetic spectrum (figure 15(*g*)). This is a typical process of field penetration and magnetic island formation, it lasts nearly 10 ms. The CIII signal increases slowly and slightly. From 0.25 s to 0.39 s, the plasma is moved towards the HFS target (figure 15(*b*)). The V_f measured by the HFS target probe array gradually becomes negative, indicating that the toroidally symmetric HFS target interacts with the plasma (figure 15(*d*)). At 0.39 s, the magnetic island width suddenly increased (figure 15(*a*)), and the $V_{\rm per}$ measured by the inner shifted channel continued to decrease (figure 15(*e*), by 47.5 GHz). Additionally, a rapid jump in the CIII signal is observed (figure 15(*f*)). This indicates a fast growth of the 3/1 magnetic island at that moment. And the boundary plasma experienced a collapse. The process lasts only 0.5 ms. The possible cause is the interaction between the plasma and the HFS target, and the carbon impurities enter plasma boundary rapidly. This destabilize the stable 3/1 magnetic island, making the island continue to grow up. Subsequently, although the magnetic island does not disappear and the boundary does not undergo periodic collapses, the edge island remains unstable and in an oscillating state (figures 15(*a*) and (*d*)). This may be the evidence that the radiative cooling effect by the accumulation of carbon impurities trigger the collapse and the instability of the magnetic island.

Finally, it is important to emphasize that the field penetration will be triggered again after the magnetic island has disappeared for a while, resulting in the periodic collapse phenomena. However, the cause of the magnetic island's disappearance is not well understood. There will be not a periodic collapse if the magnetic island always remains after the collapse. In other words, the periodic collapses are accompanied by periodic field penetration or magnetic reconnection. The magnetic island will no longer disappear after penetration when the amplitude of the RMP at the resonant surface is sufficiently large (by decreasing q_a or increasing I_c). As a result, the phenomenon of periodic collapses can no longer be observed.

5. Conclusion

In conclusion, in the J-TEXT tokamak with Ohmic-mode plasma, periodic boundary collapses were observed. The collapse is following the field penetration. During the collapse, boundary particles and heat flux were released outward through the X-point of the edge magnetic island. As the field penetration occurs, an increase in carbon impurity content happens. The magnetic island grew rapidly, this process is not entirely consistent with previously observed RMP-induced magnetic island formation. Impurities may play a role in promoting the instability of the magnetic island. After the magnetic island reaches its maximum width, it gradually decays until it disappears. The plasma then returns to its initial state until the next field penetration or collapse occurs.

Edge periodic collapses accompanied by a three-dimensional magnetic structure have been observed in both tokamak and stellarator devices. Despite potential differences in the underlying mechanisms, such phenomena can significantly affect operational stability. Observations on J-TEXT suggest that plasma–wall interactions and the edge impurity behavior play a crucial role in the stable operation of island divertors in tokamaks. Moreover, these findings provide further insights into the effect of RMP and its influence on ELMs.

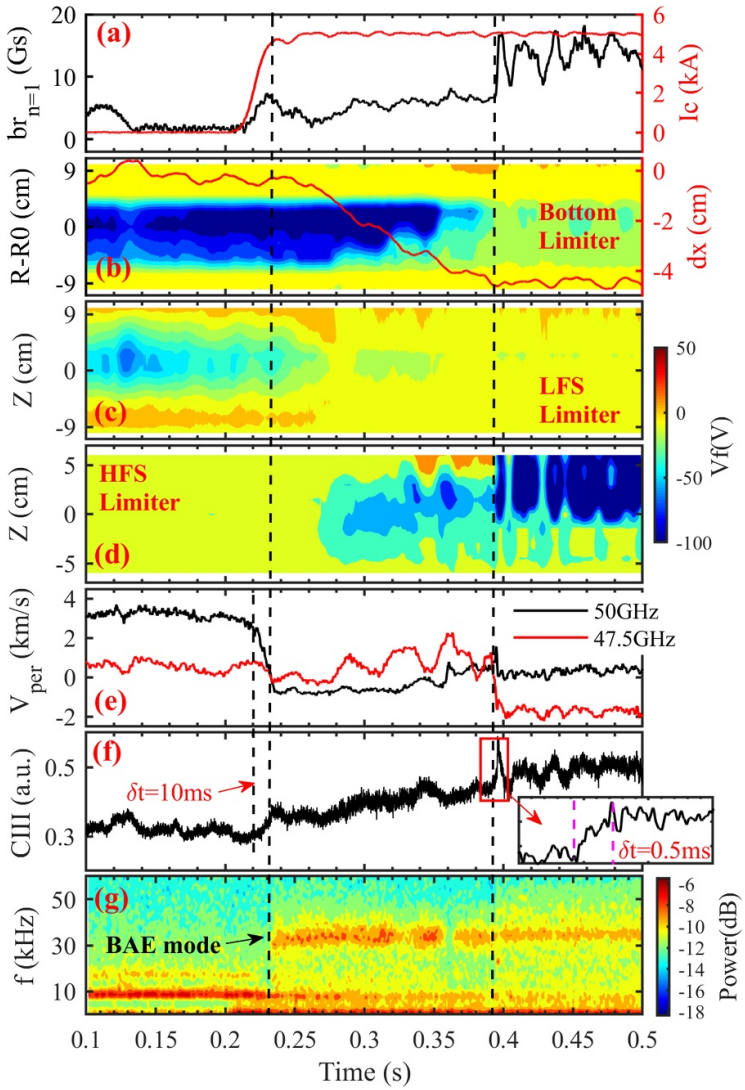

Figure 15. Discharge #1080960: Time evolution of (*a*) $\boldsymbol{b}_{r,n=1}$ and $\boldsymbol{I}_c$, (*b*) $\boldsymbol{dx}$ and $\boldsymbol{V}_f$ measured from the bottom limiter, (*c*) $\boldsymbol{V}_f$ measured from the LFS limiter, (*d*) $\boldsymbol{V}_f$ measured from the HFS limiter, (*e*) perpendicular velocity measured from DBS, the positive stand for electron diamagnetic direction, (*f*) the edge CIII signal and (*g*) perturbated magnetic spectrum.

Acknowledgments

This work was performed within the framework of the J-TEXT collaboration. This work was supported by the National Key R&D Program of China (No. 2018YFE0309101), the National Natural Science Foundation of China (No. 12375217), the Hubei International Science and Technology Cooperation Project (No. 2022EHB003), and the China Scholarship Council.

ORCID iDs

Yunfeng Liang 0000-0002-9483-6911
Zhonghe Jiang 0000-0002-4971-080X
Song Zhou 0000-0002-1407-0574
Feiyue Mao 0000-0002-7246-0036
Zhengkang Ren 0000-0001-6205-8214
Nengchao Wang 0000-0001-6797-2398

References

[1] von Goeler S., Stodiek W. and Sauthoff N. 1974 *Phys. Rev. Lett.* **33** 1201
[2] Zohm H. *et al* 1995 *Plasma Phys. Control. Fusion* **37** A313
[3] Zohm H. 1996 *Plasma Phys. Control. Fusion* **38** 105
[4] ITER Physics Expert Group on Divertor *et al* 1999 *Nucl. Fusion* **39** 2391
[5] Evans T.E. *et al* 2004 *Phys. Rev. Lett.* **92** 235003
[6] Evans T.E. *et al* 2005 *Nucl. Fusion* **45** 595
[7] Liang Y. *et al* 2007 *Phys. Rev. Lett.* **98** 265004
[8] Kirk A. *et al* 2010 *Nucl. Fusion* **50** 034008
[9] Canik J.M. *et al* 2010 *Phys. Rev. Lett.* **104** 045001
[10] Suttrop W. *et al* 2011 *Phys. Rev. Lett.* **106** 225004
[11] Sun Y.W. *et al* 2016 *Phys. Rev. Lett.* **117** 115001
[12] Liang Y. *et al* 2013 *Nucl. Fusion* **53** 073036

[13] Kobayashi T., Kobayashi M., Narushima Y., Suzuki Y., Watanabe K., Mukai K. and Hayashi Y. 2022 *Phys. Rev. Lett.* **128** 085001
[14] Wurden G.A. *et al* 2019 *46th EPS Conf. on Plasma Physics* (European Physical Society)
[15] Feng Y. *et al* 2024 *Nucl. Fusion* **64** 086027
[16] Ding Y. *et al* 2024 *Nucl. Fusion* **64** 112005
[17] Liang Y. *et al* 2019 *Nucl. Fusion* **59** 112016
[18] Chen J. *et al* 2014 *Rev. Sci. Instrum.* **85** 11D303
[19] Yang Z.J. *et al* 2012 *Rev. Sci. Instrum.* **83** 10E313
[20] Zhang X.L. *et al* 2019 *Fusion Eng. Des.* **147** 111241
[21] Han D.L., Shen C., Wang N., Li D., Mao F., Ren Z. and Ding Y. 2021 *Plasma Sci. Technol.* **23** 055104
[22] Ren X.H. *et al* 2021 *Rev. Sci. Instrum.* **92** 033545
[23] Chen Z.P. *et al* 2022 *Plasma Sci. Technol.* **24** 124008
[24] Liu L.Z., He J., Hu Q. and Zhuang G. 2015 *Plasma Phys. Control. Fusion* **57** 065007
[25] Liu L.Z. *et al* 2019 *Nucl. Fusion* **59** 126022
[26] Yang J. *et al* 2024 *Nucl. Fusion* **64** 024001
[27] Wesson J. 1997 *Tokamaks* (Clarendon)
[28] Hu Q. *et al* 2016 *Nucl. Fusion* **56** 092009
[29] Zhou S. *et al* 2024 *Nucl. Fusion* **65** 016020
[30] Liang Y. *et al* 2022 *Plasma Sci. Technol.* **24** 124021
[31] Wang N. *et al* 2014 *Nucl. Fusion* **54** 064014
[32] Loureiro N.F., Cowley S.C., Dorland W.D., Haines M.G. and Schekochihin A.A. 2005 *Phys. Rev. Lett.* **95** 235003
[33] Liang Y., Koslowski H.R., Krämer-Flecken A., Zimmermann O., Löwenbrück K., Bertschinger G. and Wolf R.C. 2007 *Nucl. Fusion* **47** L21
[34] Xu M. *et al* 2022 *Nucl. Fusion* **62** 056019
[35] Zeng S., Zhu P., Zhou R. and Escande D.F. 2022 *Nucl. Fusion* **63** 016026
[36] Xu H., Zhang H.-W., Song Y.-H., Ma Z.-W. and Wang Y.-N. 2020 *Plasma Phys. Control. Fusion* **62** 105009
[37] Wesson J.A. *et al* 1989 *Nucl. Fusion* **29** 641
[38] Suttrop W. *et al* 1997 *Nucl. Fusion* **37** 119
[39] Salzedas F., Schüller F.C. and Oomens A.A.M. (the RTP Team) 2002 *Phys. Rev. Lett.* **88** 075002
[40] White R.B., Gates D.A. and Brennan D.P. 2025 *Phys. Plasmas* **22** 022514
[41] Teng Q., Ferraro N., Gates D.A. and White R.B. 2018 *Nucl. Fusion* **58** 106024
[42] Zhang X.L. *et al* 2021 *Plasma Sci. Technol.* **23** 125101